PHYSICAL REVIEW C **69**, 025803 (2004)

Neutron capture studies on unstable ^{135}Cs for nucleosynthesis and transmutation

N. Patronis,[1] S. Dababneh,[2,*] P. A. Assimakopoulos,[1] R. Gallino,[3] M. Heil,[2] F. Käppeler,[2,†] D. Karamanis,[1] P. E. Koehler,[4] A. Mengoni,[5] and R. Plag[2]

[1]*Nuclear Physics Laboratory, Department of Physics, The University of Ioannina, 45110 Ioannina, Greece*
[2]*Forschungszentrum Karlsruhe, Institut für Kernphysik, 76021 Karlsruhe, Germany*
[3]*Dipartimento di Fisica Generale, Università di Torino and Sezione INFN di Torino, I-10125 Torino, Italy*
[4]*Physics Division, Oak Ridge National Laboratory, Oak Ridge, Tennessee 37831, USA*
[5]*CERN, 1211 Geneva 23, Switzerland*

(Received 10 November 2003; published 27 February 2004)

The neutron capture cross section of the unstable isotope ^{135}Cs was measured relative to that of gold by means of the activation method. The sample was produced by ion implantation in a high resolution mass separator and irradiated with quasimonoenergetic neutrons at 30 keV and 500 keV, using the ^{7}Li$(p,n)^{7}$Be reaction. An additional irradiation with thermal neutrons has been carried out for defining the sample mass and for measuring the half-life of ^{136}Cs. The neutron capture cross sections were determined as 164 ± 10 mb and 34.8 ± 3.0 mb at 30 keV and 500 keV, respectively, and were used to normalize the theoretically derived cross section shape. Based on these data, refined statistical model calculations were performed to obtain the (n,γ) cross sections of the short-lived isotopes ^{134}Cs and ^{136}Cs as well. Updated Maxwellian-averaged capture cross sections of all unstable Cs isotopes were calculated for a range of thermal energies characteristic of helium burning scenarios for an improved *s*-process analysis of the Xe-Cs-Ba region.

DOI: 10.1103/PhysRevC.69.025803 PACS number(s): 25.40.Lw, 27.60.+j, 97.10.Tk

I. INTRODUCTION

The neutron capture cross section of ^{135}Cs in the keV region is required for two reasons. It determines the amount of radioactive cesium in burnt fuel elements of fast reactors and it contributes to a quantitative interpretation of the isotopic Ba abundances in terms of the temperature during stellar He burning.

Nucleosynthesis by the slow neutron capture process (*s* process) is characterized by neutron capture times, which are typically much longer than the half-lives against β decay [1]. Consequently, the reaction path in the *N*-*Z* plane follows the valley of stability as sketched in Fig. 1. However, some unstable nuclei are sufficiently long lived such that neutron capture can compete with β decay. These nuclei act as branching points in the reaction path of the *s* process. Several such branchings are indicated in the example of Fig. 1. The most prominent of these branchings occurs at ^{134}Cs, whereas all others are comparably weak and have minor impact on the final Ba abundances. Apart from its strength, the main importance of the ^{134}Cs branching lies in the fact that it determines the abundance ratio of ^{134}Ba and ^{136}Ba. Both isotopes are of pure *s*-process origin since they are shielded from possible *r*-process contributions by their stable Xe isobars. Accordingly, valuable information with regard to the physical conditions during the *s* process can be obtained from the reliable quantitative description of the branching. In the present case, this refers to the proper combination of neutron density and temperature. The sensitivity to temperature results from the fact that the first excited state of ^{134}Cs starts to be populated by the hot stellar photon bath at temperatures in excess of 10^{8} K. Allowed β decay from that state results in a strong reduction of the half-life [2].

Since the specific activity of ^{134}Cs is prohibitive for direct measurements, improvement of the capture rate can be achieved by normalizing statistical model calculations at experimental cross sections for the neighboring isotopes. Accurate experimental data for the only stable isotope, ^{133}Cs, were complemented by a first measurement on ^{135}Cs by Jaag *et al.* [3] in a quasistellar neutron spectrum at the stellar thermal energy $kT\simeq25$ keV. However, recent stellar *s*-process models require neutron capture rates over a wider temperature range from $kT\simeq8$ keV to $kT\simeq26$ keV [1,4]. Therefore, in this work the neutron capture cross section was measured at two distinct neutron energies of 30 keV and 500 keV in or-

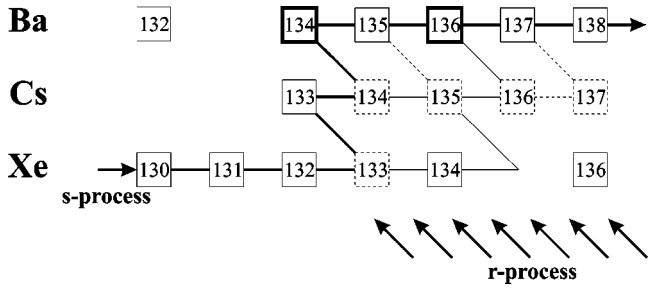

FIG. 1. The *s*-process path in the Xe-Cs-Ba region, which includes the important branching point ^{134}Cs. This branching determines the isotopic ratio of the *s*-only isotopes ^{134}Ba and ^{136}Ba, which are shielded against abundance contributions from the *r*-process region (indicated by arrows) by their stable Xe isobars. Note that ^{135}Cs is practically stable on the time scale of the *s* process, but decays afterwards and contributes to the final ^{135}Ba abundance.

*On leave from Faculty of Applied Sciences, Al-Balqa Applied University, Salt 19117, Jordan.
†Electronic address: franz.kaeppeler@ik.fzk.de

der to normalize the theoretically calculated cross section, which then can be used to obtain the required rates as a function of temperature.

An additional motivation arises from the fact that ^{135}Cs is an important fission product. Due to its large fission yield and its long half-life it contributes significantly to the long-term hazards of nuclear waste. The exact amount of ^{135}Cs at the end of the fuel cycle depends strongly on its neutron capture cross section, which governs its transmutation rate during burn-up. For thermal reactors, the (n_{th}, γ) cross section has been measured with good accuracy [5–7], but for fast reactors, e.g., for the currently investigated accelerator driven systems (ADS) [8], this cross section has to be known for neutron energies up to 1 MeV.

II. MEASUREMENTS

A. Experimental method

The neutron capture cross section of ^{135}Cs was measured relative to that of gold, using the activation technique. This technique offers the high sensitivity, which is essential since measurements on radioactive isotopes have to be carried out with very small samples in order to keep the background from radioactive decay at a manageable level. In total, four irradiations were carried out, the first three at the Karlsruhe 3.7 MV Van de Graaff accelerator and the fourth at the TRIGA reactor of the University of Mainz. The irradiations at the Van de Graaff were separated by waiting times of three months, corresponding to seven half-lives of the induced ^{136}Cs activity. In order to obtain comparable statistics, the measurement was carried out by one activation at 30 keV and two at 500 keV. Each irradiation lasted for about two weeks and was followed by two weeks of measurement of the induced activity. During the irradiation the gold reference foils (see below) were replaced approximately every three days because of the 2.7 d half-life of ^{198}Au to avoid saturation effects in the determination of the integrated neutron flux. Variations in the neutron flux were continuously monitored by a ^{6}Li-glass detector.

The last irradiation was carried out with reactor neutrons in order to define the number of ^{135}Cs nuclei in the sample via the well-known thermal neutron capture cross section [7]. In this case, a Re foil was used to monitor the neutron flux as described below. Following the reactor irradiation, the induced activity was measured using the same detector setup as for the activations at 30 keV and 500 keV. This had the advantage that sample-related corrections, the detector efficiency, and geometry effects were canceled out (Sec. III C).

B. Irradiations

The experimental setup consisted mainly of two parts, pertained to the irradiation of the sample and to the γ-ray detection system.

At the accelerator, neutrons were produced via the ^{7}Li$(p,n)^{7}$Be reaction by bombarding metallic Li targets evaporated onto a 1.0 mm thick Cu backing. Proton beam currents were typically kept between 90 and 100 μA. The targets were cooled using lateral heat conduction through the copper backing to a surrounding water channel of 8 mm inner diameter (Fig. 2). The thickness of the Li targets were 30 and 10 μm for the runs at 30 and 500 keV, respectively. The Li layers were 6 mm in diameter, equal to the sample. The Cs sample was sandwiched between gold foils, also 6 mm in diameter and 0.03 mm thick. The distance of the sample sandwich to the lithium target was 1.5 mm during the 30 keV run and 8 mm during the 500 keV run.

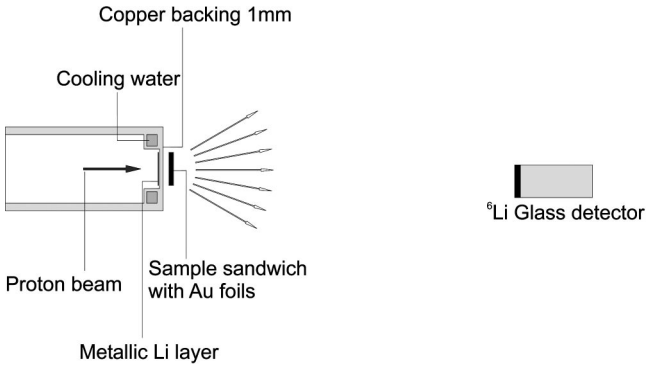

FIG. 2. Experimental setup during irradiation. The sample sandwich was located in the high flux close to the lithium target, and the distance between target and ^{6}Li-glass detector was 1 m.

Figure 2 shows also the ^{6}Li-glass detector, which was located 1 m from the target at 0° with respect to the beam axis. With this detector the proper proton energy was selected prior to the irradiations by means of a time of flight (TOF) measurement of the neutron spectrum. For this purpose, the accelerator was operated in pulsed mode. During the irradiation the detector served to measure the neutron yield at regular time intervals. This neutron flux history was used in the analysis for off-line correction of the fraction of ^{135}Cs nuclei, which decayed already during irradiation.

The main quantities concerning the irradiation of the sample at the accelerator and at the reactor are summarized in Table I.

C. Activity measurements

The induced activity of the cesium sample was measured with two Clover-type HPGe detectors (Eurisys). Each of the two detectors combines four independent *n*-type Ge crystals in a common cryostat [9]. The Clover detectors were placed face to face in close geometry (Fig. 3). The distance between the Al windows of the detectors was fixed by the sample holder at 5.2 mm. The sample was positioned exactly in the midplane of the two Clovers centered on their common axis. The individual Clover crystals were $\approx$50 mm in diameter and 70 mm long. The absolute peak efficiency of this setup for the 818.5 keV line in the decay of ^{136}Cs was $\epsilon_\gamma = (1.069 \pm 0.017) \times 10^{-1}$ [10]. The high detection efficiency of the γ spectrometer was instrumental for accumulating satisfactory statistics from the weak activities obtained with the minute ^{136}Cs sample. The detector signals were stored event by event for detailed off-line analysis using the data acquisition system MPA-WIN (FAST COMTEC).

The activity of the Au foils was measured with a 40 cm^3 *n*-type HPGe detector. The Au foils were placed 76 mm from

TABLE I. Parameters and neutron flux for the irradiations of the ^{135}Cs sample.

	30 keV	500 keV (first irradiation)	500 keV (second irradiation)	Reactor irradiation
Irradiation time	11.1d	15.4 d	13.5 d	70 min
Integrated flux (cm^{-2})	$(8.12\pm0.26)\times10^{14}$	$(1.49\pm0.07)\times10^{15}$	$(1.61\pm0.09)\times10^{15}$	$(2.19\pm0.05)\times10^{15}$
Flux monitor foils	Au	Au	Au	Re
Sets of monitor foils	5	5	3	1
Decay corrections f_B				
Monitor foils	0.861, 0.780, 0.697	0.800, 0.559, 0.674,	0.469, 0.612,	0.995 (^{185}Re)
	0.699, 0.786	0.781, 0.656	0.699	0.977 (^{185}Re)
Cs sample	0.761	0.735	0.697	0.999

the window of the detector, a distance where pileup corrections were negligibly small. In this case, the absolute peak efficiency for the 412 keV line from the decay of ^{198}Au was $\epsilon_\gamma=(2.20\pm0.03)\times10^{-3}$.

The same detector was used for measuring the Re activity after the reactor irradiation. In this case, the Re foil had to be placed at 1 m distance from the detector in order to keep the counting rate sufficiently low.

D. Neutron spectra

The neutron energy distributions in the sample were calculated from the double differential cross section of the ^{7}Li$(p,n)^7$Be reaction using a C++ computer code NYIELD based on Ref. [11]. The code was verified by comparison with the experimental neutron spectrum of Ratynski and Käppeler [12] as shown in Fig. 4 and also via the TOF measurements performed during this experiment. In all cases the calculated spectra were consistent with the measurements.

The spectrum at $E_n=30$ keV was obtained by adjusting the proton beam energy to 1892 keV, 11 keV above the reaction threshold and by using a thick Li target. At this energy, the reaction kinematics restrict the emitted neutrons to a forward cone with an opening angle of 65°. For the runs at $E_n=500$ keV, the proton energy was 2284 keV, where neutrons are emitted in all directions. At this energy, the neutron spectrum seen by the sample was determined by means of the GEANT4 Monte Carlo (MC) code [13]. The MC technique was preferred in this case since it allows one to determine the effect of the background neutrons for the specific experimental setup, including the proper angular distribution of the source neutrons. The resulting neutron spectra for the 30 keV and 500 keV runs are presented in Fig. 5.

The neutron spectrum during the reactor irradiation is composed of the true Maxwellian spectrum at thermal energies and an epithermal component with a typical $1/E_n$ behavior, which is taken into account by the resonance integral. At the irradiation position the ratio of epithermal flux with $E_n>0.4$ eV and the thermal flux was 4/70.

The values of the neutron flux during sample irradiation at 30 and 500 keV, as well as in the reactor are listed in Table I, and the calculation is described in Sec III.

E. The ^{135}Cs target

The ^{135}Cs sample used in this work was produced at Los Alamos National Laboratory with a high resolution mass separator. It was specified to contain 1.8×10^{15} ^{135}Cs atoms, corresponding to a total mass of ~400 ng, implanted in a graphite disc 0.1 mm in thickness and 6 mm in diameter. A small remaining ^{137}Cs impurity of 167 Bq could be used to monitor the sample mass throughout the measurements. The sample disk was canned in a cylindrical graphite box with 0.3 mm thick walls.

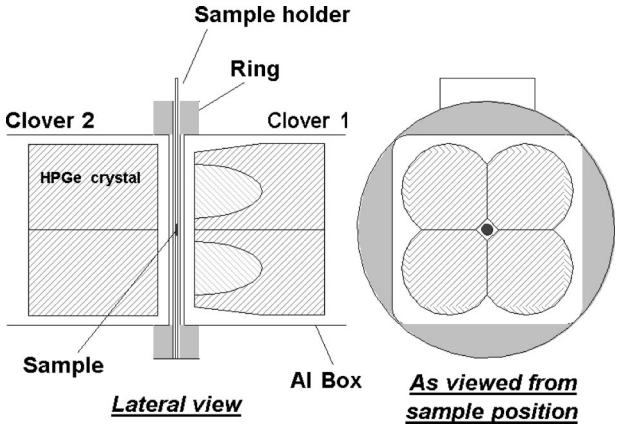

FIG. 3. Setup of the Clover detectors. The close geometry requires an exact and reproducible positioning of sample and detectors, which was achieved with a special sample holder.

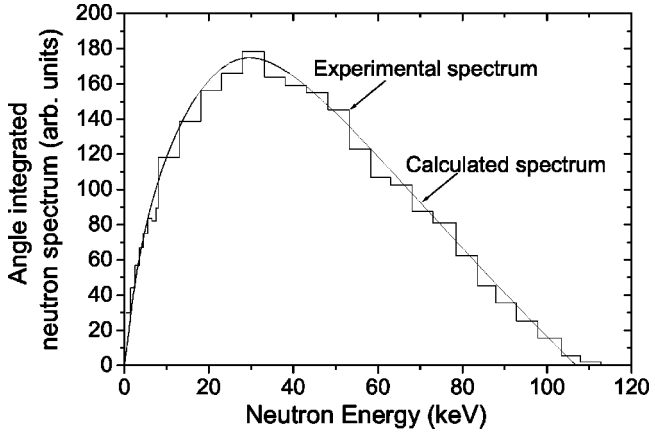

FIG. 4. The calculated neutron spectrum compared to the experimentally deduced spectrum from Ratynski and Käppeler [12].

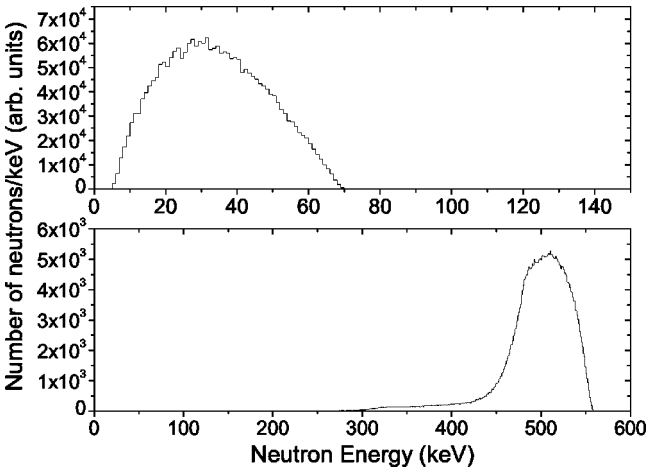

FIG. 5. The neutron energy spectra seen by the Cs sample in the irradiations at 30 keV (upper panel) and 500 keV (lower panel), as deduced with the NYIELD code and the GEANT4 calculations.

III. DATA ANALYSIS

A. Neutron flux

For each run at the accelerator, the time integrated neutron flux was measured by the induced ^{198}Au activity. Due to the geometry of the sample sandwich, the downstream Au foil could not be placed in direct contact with the cesium sample. Since only the upstream Au foil was used in the analysis, the geometry factor for extrapolation of the neutron flux to the position of the Cs sample was determined experimentally. For each energy, a special irradiation was performed by placing additional Au foils at different distances from the upstream Au reference foil. From the smooth variation with distance (Fig. 6), the correction for the neutron flux seen by the cesium sample could be determined with good accuracy.

The time integrated neutron flux

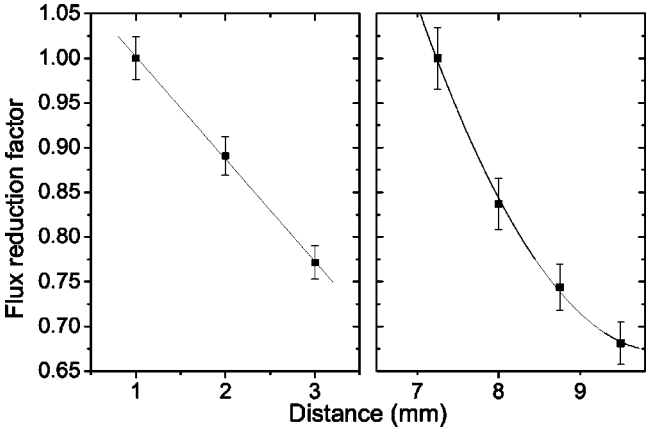

FIG. 6. Neutron flux vs distance from the copper backing of the Li target. The flux obtained from a set of gold foils was normalized to the flux measured with a foil at the nominal position used during the activations, i.e., 1 mm and 7.5 mm at 30 and 500 keV, respectively.

TABLE II. Decay properties of the product nuclei.

Product nucleus	Half-life	γ-ray energy[a] (keV)	Intensity per decay (%)
^{136}Cs[b]	13.16±0.03 d	818.5	99.7±0.06[c]
^{198}Au	2.6952±0.0002 d	411.8	95.58±0.12[d]
^{186}Re	3.7183±0.0011 d	137.2	9.42±0.06[e]
^{188}Re	17.0040±0.0022 h	155.0	15.61±0.18[f]
^{188m}Re[g]	18.59±0.04 min		

[a]Prominent γ-ray lines used in data analysis.
[b]Only the half-life of ^{136}Cs was used in data analysis (see Sec. III C).
[c]Reference [15].
[d]Reference [16].
[e]Reference [17].
[f]Reference [18].
[g]100% internal decay to ^{188}Re since the measurement was performed 20 h after irradiation when the metastable state had already decayed.

$$\Phi = \frac{\Delta N C_A C_{DT} C_{FR}}{(1 - e^{-\lambda t_m}) e^{-\lambda t_w} \sigma \epsilon I f_B N} \tag{1}$$

can be derived from the number of counts in the 412 keV line of ^{198}Au, ΔN. The factors C_A and C_{DT} correspond to the self-attenuation and dead time corrections, respectively. The factor C_{FR} stands for the correction of the neutron flux from the value measured by the upstream gold foil to the position of the Cs sample (Fig. 6). In the denominator, the time factor f_B corrects for the decay during activation as well as the effect of time variations in the neutron flux [14]. The measuring time and the time interval between the end of the irradiation and the beginning of the measurement are denoted as t_m and t_w, respectively. The factors N, λ, ϵ, and I are the number of gold atoms in the reference foil, the decay rate of ^{198}Au, the absolute efficiency of the HPGe detector, and the intensity of the 412 keV line, respectively. The cross section of the ^{197}Au(n,γ) reaction, which was used as a reference, was obtained from the ENDF/B-VI database after normalization to the experimental 30 keV value of Ratynski and Käppeler [12], and by folding with the neutron beam energy distribution (Fig. 5). The normalization factor for the ENDF/B-VI gold cross section was 0.958. The γ-ray intensities and half-lives used in the analysis are summarized in Table II.

The thermal neutron flux in the last irradiation was determined from the concomitant activation of a Re foil. Rhenium was chosen because the ratios of resonance integrals and thermal cross sections, $r = I_{res}/\sigma_{th}$, for two stable isotopes, ^{185}Re and ^{187}Re, are 15.3 and 3.9, respectively [19]—above and below that of ^{135}Cs (r=4.6) [7]. This permits an accurate determination of the thermal and epithermal part of the reactor spectrum. The nuclear data used for the analysis of the reactor irradiation are listed in Table III.

TABLE III. Adopted thermal neutron capture cross sections and resonance integrals.

Reaction	σ_{th} (barn)	I_{res} (barn)	Reference
^{135}Cs$(n,\gamma)^{136}$Cs	8.3±0.3	37.9±2.7	[7]
^{185}Re$(n,\gamma)^{186}$Re	112±2.0	1717±50	[19]
^{187}Re$(n,\gamma)^{188}$Re	76.4±1.0	300±20	[19]
^{187}Re$(n,\gamma)^{188m}$Re	2.8±0.1		[19]

B. Activity measurements

The activity of the Cs sample was measured with the Clover detector system as described in Sec. II C. The data were recorded in event-by-event mode, thus achieving great flexibility in off-line analysis.

Three modes of reconstruction were tested for the analysis of the data [10].

In direct mode, each Ge crystal of the Clover system is considered as an individual detector. In this mode, the full energy peak efficiency is equal to the sum of the photopeak efficiencies of each of the eight detectors.

The addback mode, in which coincident signals are added. In this way cross talk effects between neighboring crystals due to Compton scattering or pair production are restored, thus enhancing the photopeak efficiency. The addback mode of detection is very efficient for large source-to-detector distances, but is not useful in the close geometry of the present experiment due to the dominance of summing effects.

The coincidence mode, in which signals are only registered if any of the eight ADCs recorded a signal in a certain energy interval. This mode selects cascade transitions and leads to a strong background reduction at the price of a considerable loss in detection efficiency. This is illustrated in the lower panel of Fig. 7, which shows the coincidence spectrum taken in the 30 keV run with the gate set on the 1048 keV transition in the ^{136}Cs decay: Even the weakest transitions with a 3% intensity per decay can be clearly identified. The presence of some lines, which cannot be assigned to the decay of ^{136}Cs, are artifacts due to Compton coincidences [10].

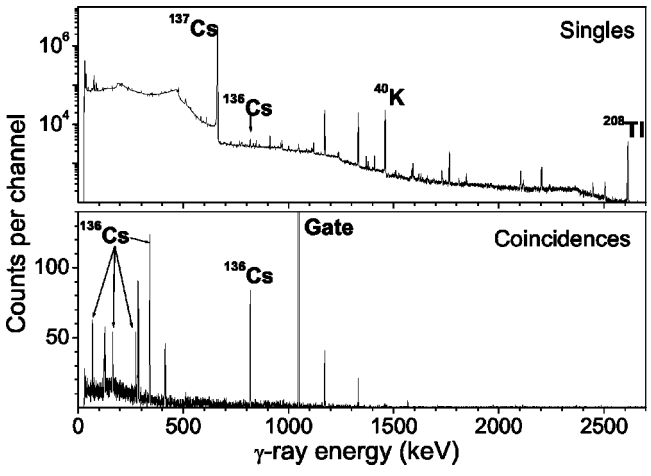

FIG. 7. The γ-ray spectra of the 30 keV run measured in singles mode (upper panel) compared to the one obtained in coincidence mode by off-line analysis (lower panel). The coincidence window at 1048 keV is also indicated. Both spectra are in direct mode of operation.

TABLE IV. Compilation of uncertainties.

Source of uncertainty	Uncertainty (%) 30 keV	500 keV
Gold cross section	2	3
Measurement of fast flux	3.2	5.1
Counting statistics	3.6	5.8
Time factors	<0.5	
^{135}Cs, thermal capture cross section	3.6	
^{135}Cs, effect of resonance integral	(0.1)	
Measurement of thermal flux including contributions from	2.1	
^{185}Re, thermal capture cross section	(1.8)	
^{187}Re, thermal capture cross section	(1.3)	
^{185}Re, effect of resonance integral	(<0.1)	
^{187}Re, effect of resonance integral	(0.2)	
Total uncertainty of cross section	6.1	8.6

Although the peak-to-background ratio is much better in the coincidence spectrum, the statistical uncertainty was smaller in the spectrum taken in singles mode. In any case, the results obtained with both modes were consistent within the statistical uncertainties.

The uncertainties in the final cross sections were derived from the singles mode of detection and are summarized in Table IV. Systematic and statistical uncertainties contribute almost equally at both energies. In the runs at 500 keV the neutron flux is practically isotropic, which implies a somewhat larger flux uncertainty due to the positioning of the sample (Fig. 6). The resonance integrals of the three isotopes irradiated in the reactor have only a small impact on the final uncertainties.

C. Combination with thermal data

The combination of the keV cross section measurements with the one at thermal energies had the advantage that several parameters canceled out in the final expression,

$$\sigma = \frac{(\sigma)_r(\Phi)_r(f_B)_r(1-e^{-\lambda(t_m)_r})\Delta N e^{-\lambda(t_w)_r} C_{DT}}{\Phi(\Delta N)_r(1-e^{-\lambda t_m})e^{-\lambda t_w} f_B (C_{DT})_r}, \qquad (2)$$

where the subscript r refers to the reactor irradiation. In this way, the systematical uncertainties for the γ efficiency of the Ge detectors, for the intensity of the ^{136}Cs line, as well as for the corrections of the self-attenuation and summing effects could be eliminated. This holds also for the effect of a possible inhomogeneity of the ^{135}Cs sample. The condition that the counting geometry was accurately reproduced in the activity measurements was verified by the design of the sample holder as well as by the counting rate of the 662 keV line from the ^{137}Cs contamination in the sample.

TABLE V. The measured and evaluated capture cross sections (in mb).

Energy (keV)	Experiment	(ENDF/B-VI)	Ratio
30 keV	164±10	204	0.804
500 keV	34.8±3.0	43.6	0.798

IV. RESULTS AND DISCUSSION

A. Differential cross sections

For the investigated energy spectra (Fig. 5) the neutron capture cross sections of the unstable isotope ^{135}Cs were found to be 164±10 and 34.8±3.0 mb at 30 and 500 keV, respectively. For direct comparison, the cross section provided in the ENDF/B-VI library [32] was folded with the experimental neutron spectra. As shown in Table V the experimental results for both energies are 20% lower than the calculated values of the ENDF/B-VI database, thus confirming the shape of the evaluated cross section (Fig. 8). Normalization of the ENDF/B-VI data to the measured values at 30 and 500 keV yields the energy-dependent cross section between these limits with the experimental uncertainty. For extrapolation to lower energies, i.e., into the region from 1 to 30 keV, an additional uncertainty was estimated from the slightly different energy dependence of the ENDF/B-VI data and the Hauser-Feshbach statistical model (HFSM) calculations performed in this work (Fig. 8). The extrapolation uncertainty towards higher energies was obtained in a similar way. The resulting differential ^{135}Cs cross section is given in Table VI.

B. Half-life of ^{136}Cs

Discrepancies in the half-life of ^{136}Cs between the values of Katoh *et al.* [7] (12.63±0.04 d) and the most recent compilation [15] (13.16±0.03 d) prompted us to resolve this problem by measuring the decay curve after the reactor activation. The intensities of the 819 and 1048 keV lines from the decay of ^{136}Cs were determined daily during a period of 37 d (Fig. 9). In all these runs, a statistical uncertainty of less than 1% was achieved. The fit of the respective decay curves provided perfectly consistent results for both transitions (Table VII). The combined value of 13.04±0.03 d is compatible with Ref. [15] but deviates from the measurement of Katoh *et al.* [7] by 10 standard deviations.

Particular attention was paid to the claim [7] that previous half-life measurements may have had problems with the pileup corrections. At the start of this measurement, the count rate of the Clover detectors was 2.3 kHz, corresponding to ~285 counts/sec for each of the eight independent Ge crystals. This rate was sufficiently low such that the pileup correction is negligible.

TABLE VI. The ^{135}Cs$(n,\gamma)^{136}$Cs cross section obtained by normalizing the present calculation to the experimental results.

Energy (keV)	Cross section (mb)
1	1561 ± 156
3	676 ± 68
5	482 ± 48
10	317 ± 28
20	213 ± 17
30	160 ± 10
40	133 ± 9
50	115 ± 8
60	104 ± 7
80	88.2 ± 6.2
100	78.3 ± 5.5
200	56.3 ± 4.0
300	43.2 ± 3.4
400	37.8 ± 3.2
500	34.9 ± 3.0
1000	30.6 ± 3.8

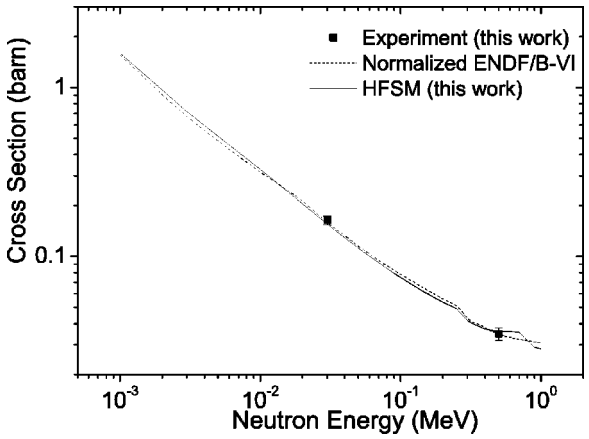

FIG. 8. The experimental and the evaluated results for the ^{135}Cs$(n,\gamma)^{136}$Cs cross section. The evaluated data have been normalized to the experimental points.

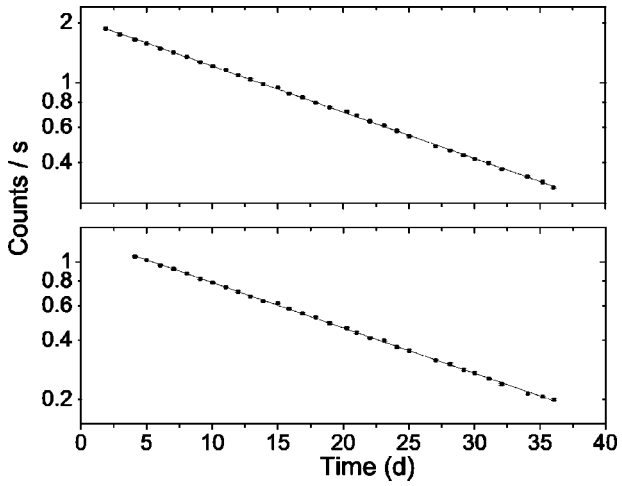

FIG. 9. The decay curve of ^{136}Cs obtained from the counting rates of the transitions at 819 keV and 1048 keV (upper and lower panel, respectively).

TABLE VII. Measured half-life of ^{136}Cs.

Transition energy (keV)	Half-life (d)
818.5	13.04±0.03
1048	13.04±0.04

C. Transmutation of ^{135}Cs

Due to its high fission yield, ^{135}Cs is one of the important long-lived fission products. For example, it is accumulated at a rate of 1.4 kg per Terawatt-hour-electric in pressurized water reactors [20]. Therefore the transmutation of ^{135}Cs via neutron capture to the short-lived ^{136}Cs is of primary interest. While the thermal cross section was known to good accuracy, only theoretical data were available in the relevant energy region of fast reactors in general and for the presently studied ADS [8], in particular. The energy spectra of such systems, which are considered as efficient waste burners, peak typically near 1 MeV. Accordingly, experimental information in this energy range is important for the neutronics and the incineration features of ADS.

The results presented here show that the keV neutron capture cross section of ^{135}Cs is 20% smaller than adopted in the ENDF/B-VI library. This implies that the transmutation efficiency of ^{135}Cs in ADS will be ~20% lower than previously assumed.

V. ASTROPHYSICAL ASPECTS

A. Maxwellian-averaged cross sections

For the use in stellar models, Maxwellian-averaged cross sections

$$\frac{\langle\sigma v\rangle}{v_T} = \frac{2}{\sqrt{\pi}} \frac{\int_0^\infty \sigma(E_n) E_n \exp(-E_n/kT) dE_n}{\int_0^\infty E_n \exp(-E_n/kT) dE_n} \quad (3)$$

were determined in a range of thermal energies typical for various *s*-process scenarios. For a complete picture of the isotopic abundance pattern produced in the *s* process (Fig. 1), the experimental data for ^{133}Cs and ^{135}Cs had to be complemented by the corresponding data of the remaining unstable Cs isotopes with $A=134, 136$, and 137.

1. Experimental data

The values for ^{135}Cs are based on the results of this work (Table VI). The only previous measurement by Jaag *et al.* was performed with the same sample, but in a quasistellar neutron spectrum [3]. The obvious difference between the Maxwellian-averaged (n,γ) cross section at $kT=30$ keV of 198±17 mb reported in Ref. [3] and the present value of 160±10 mb is due to the reference data used in evaluating the activation at thermal energies. In both experiments, the number of ^{135}Cs atoms were determined by means of an activation in the same irradiation position of the TRIGA reactor of the University of Mainz. In the analysis, improved neutron capture data could be used for the thermal cross section as well as for the resonance integral [7]. Especially the value of the resonance integral was significantly different (37.9±2.7 barn compared to 61.7±2.3 barn [19] used by Jaag *et al.*), whereas the thermal value was consistent within uncertainties (8.3±0.3 barn compared to 8.7±0.5 barn [19]). Under the realistic assumption that the neutron spectrum was identical in both activations, the previous activation can be corrected with respect to the thermal data. In this case, one obtains a stellar 30 keV cross section of 176±15 mb, in agreement with the present result.

TABLE VIII. The Maxwellian-averaged neutron capture cross section for thermal energies characteristic of the He burning scenarios.

	^{133}Cs		^{134}Cs		^{135}Cs		^{136}Cs		^{137}Cs	
Thermal energy (keV)	$\langle\sigma\rangle$ (mb)	SEF	$\langle\sigma\rangle$ (mb)	SEF	$\langle\sigma\rangle$ (mb)	SEF	$\langle\sigma\rangle$ (mb)	SEF	$\langle\sigma\rangle$ (mb)	SEF
5	1365±56	1	2421±218	0.989	522±52	1	558	1	15	1
8			1765±159	0.982	382±36	1	408	1	11	1
10	931±38	1	1520±137	0.982	329±30	1	352	1	8.9	1
15	745±31	0.999	1159±104	0.985	251±21	1	269	1	6.6	1
20	636±26	0.995	955±86	0.989	208±17	1	222	1	5.3	1
25	563±23	0.989	820±74	0.993	180±13	1	191	1	4.5	1
30	509±21	0.981	724±65	0.997	160±10	1	169	1	4.0	1
40	434±18	0.961	593±53	1.005	134±8.7	0.993	138	1	3.2	1
50	384±16	0.938	509±46	1.013	117±8.2	0.998	118	1	2.8	1
60	347±14	0.917	450±41	1.019	105±7.3	0.995	104	1	2.5	1
80	296±12	0.880	372±33	1.030	88.9±6.2	0.986	85	1	2.1	1
100	262±11	0.850	323±29	1.038	78.7±5.7	0.975	73	1	1.8	1

The corresponding values for the only stable isotope, ^{133}Cs, were adopted from the compilation of Ref. [21], which made use of the available experimental data.

Table VIII includes also the stellar enhancement factors (SEF), a correction that accounts for the fact that low lying excited states are thermally populated at the *s*-process temperatures, which can affect the total reaction rate. For ^{133}Cs, these values were taken from Ref. [21] as well.

2. Calculated cross sections

For determining the cross sections of the remaining unstable isotopes, a series of calculations has been performed in the framework of the HFSM theory of nuclear reactions. For the mass and energy range considered here, the assumption of the compound nucleus reaction mechanism, on which the HFSM is based, is assumed to be justified, although this may imply an additional uncertainty for the neutron magic isotope ^{137}Cs.

Two sets of calculations using the same HFSM theory but different parametrizations have been considered, based on the NON-SMOKER code [22] and on a code developed at ENEA [33]. The basic expression for the neutron capture cross section in HFSM is the following:

$$\sigma_{n,\gamma}(E_n) = \frac{\pi}{k_n^2}\sum_J g_J \frac{\sum_{ls} T_{n,ls} T_\gamma^J}{\sum_{ls} T_{n,ls} + \sum_{n',l's'} T_{n',l's'} + T_\gamma^J} W_{n,\gamma}^J.$$

The neutron transmission coefficients T_n for all the states in the entrance channel as well as in the exit inelastic channels n' are calculated as solutions of the two-body Schrödinger equation for a complex optical potential. Different optical model parameter (OMP) sets have been considered in the HFSM calculations with a final choice for the Moldauer OMP [23] which better reproduced the available neutron strength functions [19] in the mass region under consideration here. For excited target states, considered in the calculation of stellar cross sections, superelastic neutron emission channels have been included.

The T_γ^J transmission coefficients for each γ transition have been calculated using giant dipole resonance parameters, and experimentally known discrete nuclear levels. For transitions leading to states above the known discrete levels, the nuclear level density $\rho(E)$ is needed. A constant-temperature model fit, matched to the Fermi gas model with pairing correlations and corrected for shell inhomogeneities at excitation energies close to the neutron binding energy, has been adopted for the calculation of $\rho(E)$. Finally, the level width fluctuation correction factor $W_{n,\gamma}^J$ has been calculated using Lynn's prescriptions [24].

The different parametrizations of the HFSM theory lead to different results in the cross sections of the cesium isotopes. In particular, the Maxwellian-averaged cross sections at 30 keV of ^{134}Cs, the nucleus of major concern here, differ by 40%. However, the cross section ratios $\sigma(134)/\sigma(135)$ and $\sigma(133)/\sigma(135)$ were consistent within 14%. In combination with the experimental results for ^{133}Cs and ^{135}Cs, this provides a reliable way for determining the Maxwellian-averaged cross section of ^{134}Cs by normalizing our calculated cross section by means of the experimental data for ^{133}Cs and ^{135}Cs. The normalization was using the present HFSM calculations, which agreed better to the experimental $\sigma(133)/\sigma(135)$ ratio. The results presented in Table VIII are estimated to carry an uncertainty of 9% resulting from the 5% difference between the results obtained by normalizing to ^{133}Cs and ^{135}Cs, respectively, and from the experimental uncertainties of the ^{133}Cs and ^{135}Cs cross sections.

The present results for ^{134}Cs confirm the previously recommended values [21], but the uncertainty was reduced by more than a factor of 2.

The resulting cross sections for the higher isotopes, which were eventually adopted for the discussion of the astrophysical implications, are given in Table VIII. The SEFs have been calculated considering thermal populations of the first five excited states in each target nucleus. For the temperatures considered here, kT up to 100 keV, this has been verified to be sufficient to include all significant contributions to the stellar rates.

These results were used to update the *s*-process analyses presented in Refs. [25–28].

B. The *s*-process branching at ^{134}Cs

The neutron capture flow through the Xe-Cs-Ba isotopes (Fig. 1) exhibits branchings at ^{133}Xe, ^{134}Cs, ^{135}Cs, and ^{136}Cs. For all these cases, the stellar β-decay rates differ from the respective laboratory rates [2], but only ^{134}Cs acts as a true branching point with significant competition between β decay and neutron capture. The strength of this branching is reflected by the relative abundances of the two *s*-only isotopes ^{134}Ba and ^{136}Ba, which are shielded against possible *r*-process contributions by their stable Xe isobars. Nevertheless, the other branchings should be included, at least in studies with *s*-process models for thermally pulsing asymptotic giant branch (AGB) stars, where the neutron density in He shell flashes exceeds 10^{10} cm^{-3} (see below). Only the electron capture branch in the decay of ^{134}Cs is always less than 10^{-3} and can, therefore, be neglected.

The temperature dependence of the ^{134}Cs decay makes this branching a potential *s*-process thermometer. In terms of the static picture of the classical *s*-process approach [29], the present data do not affect the discussion presented in Refs. [3,25]. This means that the branching at ^{134}Cs is too weak and the minor branchings remain marginal because of the comparably low neutron density limit of about 5×10^8 predicted by the classical approach. Hence, the ^{134}Ba/^{136}Ba ratio is always overestimated unless the decay rate of ^{134}Cs is reduced by a factor of 3 [1].

It was shown that this problem is resolved if the ^{134}Cs branching is treated in the frame of stellar models for helium shell burning in thermally pulsing, low mass AGB stars [4,30]. In these stars the neutron supply results from the interplay of the dominant ^{13}C$(\alpha,n)^{16}$O reaction and a weaker contribution from the ^{22}Ne$(\alpha,n)^{25}$Mg reaction. During the interpulse period between He shell flashes, a neutron density of less than 10^7 cm^{-3} is maintained in the ^{13}C pocket, a thin layer in the He shell, where the ^{13}C source operates under

TABLE IX. Ba abundances relative to the solar values obtained from stellar model calculations using previously recommended Cs cross sections [21] and the values of this work.

	Previous data	Present results
^{134}Ba	1.140	1.158
^{135}Ba[a]	0.264	0.293
^{136}Ba	1.074	1.065
^{137}Ba[a]	0.628	0.620
^{138}Ba	0.905	0.904
^{140}Ce	0.914	0.924
^{150}Sm[b]	1.00	1.00

[a]Including the radiogenic components from the decay of ^{135}Cs and ^{137}Cs, respectively.
[b]Abundance distributions normalized to ^{150}Sm.

radiative conditions and at comparably low temperatures of $kT \simeq 8$ keV. When a sufficiently high temperature is reached at the bottom of the He burning zone, the ^{22}Ne source is activated during the following He shell flash. Though the total neutron exposure is smaller than contributed by the ^{13}C$(\alpha,n)^{16}$O reaction because the ^{22}Ne source is limited to a few years, much higher neutron densities of the order 10^{10} cm^{-3} are reached at higher temperatures of $kT \simeq 23$ keV during this highly convective instability.

Model calculations for stars of 1.5 and $3M_{\odot}$ were carried out using the previously recommended Cs cross sections [21] and the present results of Table VIII. The average of the resulting abundances has been shown to reproduce the abundance distribution in the solar system remarkably well [31]. The effect of the Cs cross sections and of the branchings at ^{134}Cs and ^{136}Cs are reflected by the differences of the isotopic Ba abundances, in particular, by the abundance ratio of the *s*-only isotopes ^{134}Ba and ^{136}Ba.

The resulting Ba abundances relative to the solar values are compared in Table IX. It is interesting to note that almost as much ^{135}Cs is ejected in the AGB winds as ^{135}Ba. There is even a non-negligible radiogenic contribution to ^{137}Ba from the ^{137}Cs produced during the He shell flash, when peak neutron densities of about 10^{10} cm^{-3} are reached. The new cross sections lead to comparably small changes, which are mostly due to the higher ^{134}Cs cross section. Nevertheless, the improved accuracy of the Cs cross sections puts these values on much firmer grounds. For example, this aspect is relevant for the interpretation of isotope patterns of the SiC mainstream presolar grains which originate from the mass loosing envelopes of AGB stars.

VI. CONCLUSIONS

In this work the neutron capture cross section of the unstable isotope ^{135}Cs was measured via the activation technique at 30 keV and 500 keV, by irradiation in quasimonoenergetic neutron fields. The measurements confirm the cross section shape predicted by the ENDF/B-VI database, but normalization to the present results show that the absolute value must be lowered by 20%.

This result will put the claims for the transmutation of the long-lived fission product ^{135}Cs on safe grounds, presumably yielding a somewhat lower rate of incineration than previously assumed.

During this experiment, the half-life of ^{136}Cs was measured to be 13.04 ± 0.03 d, in fair agreement with a recent compilation [15], but in contradiction with the latest experimental value [7].

Improved Maxwellian-averaged cross sections were derived for the unstable Cs isotopes in the mass region $134 \leqslant A \leqslant 137$, in particular, for the important *s*-process branching point ^{134}Cs and ^{135}Cs. The effect of the new cross sections on the isotopic Ba abundances was studied in model calculations for thermally pulsing, low mass AGB stars, but only small variations were found.

ACKNOWLEDGMENTS

We thank D. Roller, E.-P. Knaetsch, and W. Seith for their support during the measurement at the Van de Graaff accelerator as well as G. Rupp for his excellent technical assistance. We are indebted to I. Dillmann, O. Arndt, and the staff of the TRIGA reactor of the University of Mainz for their efficient help during the irradiation with thermal neutrons. N.P. also appreciates the useful discussions with S. Harissopoulos. This work was supported through the EU Contract No. FIKW-CT-2000-00107 as well as by the Italian FIRB-MIUR Project "The astrophysical origin of the heavy elements beyond Fe."

[1] F. Käppeler, Prog. Part. Nucl. Phys. **43**, 419 (1999).
[2] K. Takahashi and K. Yokoi, At. Data Nucl. Data Tables **36**, 375 (1987).
[3] S. Jaag, F. Käppeler, and P. Koehler, Nucl. Phys. **A621**, 247c (1997).
[4] M. Busso, R. Gallino, and G. J. Wasserburg, Annu. Rev. Astron. Astrophys. **37**, 239 (1999).
[5] N. Sugarman, Phys. Rev. **75**, 1473 (1949).
[6] A. P. Baerg, F. Brown, and M. Lounsbury, Can. J. Phys. **36**, 863 (1958).
[7] T. Katoh, S. Nakamura, H. Harada, Y. Hatsukawa, N. Shinohara, K. Hata, K. Kobayashi, S. Motoishi, and M. Tanase, Nucl. Sci. Technol. **34**, 431 (1997).
[8] C. Rubbia *et al.*, CERN Technical Report No. CERN/AT-95-44-ET, 1995.
[9] G. Duchène, F. A. Beck, P. J. Twin, G. de France, D. Curien, L. Han, C. W. Beausang, M. A. Bentley, P. J. Nolan, and J. Simpson, Nucl. Instrum. Methods Phys. Res. A **432**, 90 (1999).
[10] S. Dababneh, N. Patronis, P. A. Assimakopoulos, J. Görres, M. Heil, F. Käppeler, D. Karamanis, S. O'Brien, and R. Reifarth, Nucl. Instrum. Methods Phys. Res. A (in press).

[11] C. L. Lee and X.-L. Zhou, Nucl. Instrum. Methods Phys. Res. B **152**, 1 (1999).
[12] W. Ratynski and F. Käppeler, Phys. Rev. C **37**, 595 (1988).
[13] Geant4-Collaboration, the GEANT4 Monte Carlo toolkit for the simulation of the passage of particles through matter, http://wwwinfo.cern.ch/asd/geant4/geant.html
[14] H. Beer and F. Käppeler, Phys. Rev. C **21**, 534 (1980).
[15] A. A. Sonzogni, Nucl. Data Sheets **95**, 837 (2002).
[16] Zhou Chunmei, Nucl. Data Sheets **95**, 59 (2002).
[17] Coral M. Baglin, Nucl. Data Sheets **82**, 1 (1997).
[18] Balraj Singh, Nucl. Data Sheets **95**, 387 (2002).
[19] J. F. Mughabghab, *Neutron Cross Sections* (Academic Press, New York, 1984), Vol. 1, Part B.
[20] The n_TOF Collaboration, CERN Technical Report No. CERN/SPSC 99-8 SPSC/P 310, 1999.
[21] Z. Y. Bao, H. Beer, F. Käppeler, F. Voss, K. Wisshak, and T. Rauscher, At. Data Nucl. Data Tables **76**, 70 (2000).
[22] T. Rauscher and F.-K. Thielemann, At. Data Nucl. Data Tables **75**, 1 (2000).
[23] P. A. Moldauer, Nucl. Phys. **47**, 65 (1963).
[24] J. E. Lynn, *The Theory of Neutron Resonance Reactions* (Oxford University Press, Oxford, 1968).
[25] F. Voss, K. Wisshak, K. Guber, and F. Käppeler, Phys. Rev. C **50**, 2582 (1994).
[26] P. E. Koehler, R. R. Spencer, R. R. Winters, K. H. Guber, J. A. Harvey, N. W. Hill, and M. S. Smith, Phys. Rev. C **54**, 1463 (1996).
[27] P. E. Koehler, R. R. Spencer, R. R. Winters, K. H. Guber, J. A. Harvey, N. W. Hill, and M. S. Smith, Nucl. Phys. **A621**, 258c (1997).
[28] P. Mutti, F. Corvi, K. Athanassopoulos, and H. Beer, Nucl. Phys. **A621**, 262c (1997).
[29] F. Käppeler, H. Beer, and K. Wisshak, Rep. Prog. Phys. **52**, 945 (1989).
[30] R. Gallino, C. Arlandini, M. Busso, M. Lugaro, C. Travaglio, O. Straniero, A. Chieffi, and M. Limongi, Astrophys. J. **497**, 388 (1998).
[31] C. Arlandini, F. Käppeler, K. Wisshak, R. Gallino, M. Lugaro, M. Busso, and O. Straniero, Astrophys. J. **525**, 886 (1999).
[32] See http://www.nndc.bnl.gov/nndc/endf/endfintro.html
[33] A. Mengoni (unpublished).